

Million-atom heat transport simulations of polycrystalline graphene approaching first-principles accuracy enabled by neuroevolution potential on desktop GPUs

Xiaoye Zhou,¹ Yuqi Liu,¹ Benrui Tang,¹ Junyuan Wang,¹ Haikuan Dong,^{1,*} Xiaoming Xiu,^{1,†} Shunda Chen,^{2,‡} and Zheyong Fan^{1,§}

¹*College of Physical Science and Technology, Bohai University, Jinzhou 121013, P. R. China*

²*Department of Civil and Environmental Engineering,
George Washington University, Washington, DC 20052, USA*

(Dated: October 21, 2024)

First-principles molecular dynamics simulations of heat transport in systems with large-scale structural features are challenging due to their high computational cost. Here, using polycrystalline graphene as a case study, we demonstrate the feasibility of simulating heat transport with near first-principles accuracy in systems containing over 1.4 million atoms, achievable even with consumer desktop GPUs. This is enabled by the highly efficient neuroevolution potential (NEP) approach, as implemented in the open-source GPUMD package. Leveraging the NEP model’s accuracy and efficiency, we quantify the reduction in thermal conductivity of polycrystalline graphene due to grain boundaries with varying grain sizes, resolving contributions from in-plane and out-of-plane (flexural) phonon modes. Additionally, we find that grain boundaries can lead to finite thermal conductivity even under significant tensile strain, in contrast to the divergent behavior observed in pristine graphene under similar conditions, indicating that grain boundaries may play a crucial role in thermal transport in low-dimensional momentum-conserving systems. These findings could offer insights for interpreting experimental observations, given the widespread presence of both large-scale grain boundaries and external strains in real materials. The demonstrated ability to simulate millions of atoms with near-first-principles accuracy on consumer desktop GPUs using the NEP approach will help make large-scale high-fidelity atomistic simulations more accessible to the broader research community.

I. INTRODUCTION

Since the pioneering work by Sosso *et al.* [1], which employed the Behler-Parrinello neural network potential [2] to study heat transport in phase-change materials, machine-learned potentials (MLPs) have gradually gained popularity in studying heat transport in various materials [3]. However, most previous works have focused on relatively simple systems, such as three-dimensional crystals [4–8], two-dimensional and layered materials [9–13], amorphous materials [14–18], simple liquids [19, 20], and heterojunctions [21, 22]. These systems typically involve relatively small structural features and are computationally manageable with MLPs. To date, no applications of MLPs have been reported for studying heat transport in large-scale polycrystalline systems, mainly due to the higher computational cost of most MLPs compared to traditional empirical potentials. In this work, we address this gap by demonstrating the feasibility of MLPs in studying heat transport in large-scale polycrystalline graphene systems, containing up to 1 438 236 atoms, which can be simulated even on consumer desktop GPUs. This is enabled by the highly efficient neuroevolution potential (NEP) approach [23–25] as implemented in the open-source GPUMD package [26].

Several MLPs have been developed for carbon-based systems [27–31], exploring various properties such as thermal and mechanical behavior. Here, we utilize our previously developed general-purpose NEP model for carbon systems [31], which has already been applied to study thermal and thermoelectric transport in a graphene antidot lattice with 187 200 atoms. First, we benchmark the computational performance of this NEP model compared to typical MLPs for carbon systems. Next, we validate the accuracy of the NEP model by predicting the grain boundary energies for various tilt angles. Finally, we apply this NEP model in molecular dynamics (MD) simulations to investigate heat transport in polycrystalline graphene with different grain sizes, quantifying the reduction and the scaling of the thermal conductivity with respect to the average grain size. We also resolve the contributions from the in-plane and out-of-plane (flexural) phonon modes. Additionally, we investigate the effects of external tensile strain on the thermal conductivity of polycrystalline graphene, finding that the presence of grain boundaries could effectively suppress the thermal conductivity divergence as observed in pristine graphene under similar conditions [32–34]. This suggests that grain boundaries, along with asymmetric interatomic interactions [35–39] and nearly integrable dynamics [40–42], may play an important role in thermal transport in low-dimensional momentum-conserving systems [43–46]. These findings could provide valuable insights for interpreting experimental observations in real materials that feature both large-scale grain boundaries and external strains. This work demonstrates that the NEP

* donghaikuan@163.com

† xiuxiaomingdl@126.com

‡ phychemsd@gmail.com

§ brucenju@gmail.com

approach enables highly efficient million-atom atomistic simulations approaching first-principles accuracy, making such large-scale studies more accessible to the broader research community using either high-performance computing resources or consumer desktop GPUs.

II. MODELS AND METHODS

A. Simulation models for polycrystalline graphene

We used the polycrystalline graphene samples from Ref. 47, constructed using a phase-field crystal model [48]. The grain size, d , is defined as $d = (A/n)^{1/2}$, where A is the total area of the graphene plane and n is the number of grains comprising the plane. We considered four system sizes: 22 464 atoms ($A = 24.3 \times 24.3 \text{ nm}^2$), 89 858 atoms ($A = 48.5 \times 48.5 \text{ nm}^2$), 359 502 atoms ($A = 96.9 \times 97.0 \text{ nm}^2$), and 1 438 236 atoms ($A = 193.8 \times 193.9 \text{ nm}^2$). Each sample was initially prepared with 16 randomly placed and oriented crystallites; however, after relaxation, the final number of grains was typically smaller than 16. For each system size, we prepared several independent samples with varying grain distributions: 7, 4, 2, and 3 samples, averaging over which yielded four effective grain sizes of 8 nm ($A = 24.3 \times 24.3 \text{ nm}^2$), 14 nm ($A = 48.5 \times 48.5 \text{ nm}^2$), 26 nm ($A = 96.9 \times 97.0 \text{ nm}^2$), and 50 nm ($A = 193.8 \times 193.9 \text{ nm}^2$), respectively. Figure 1 illustrates the polycrystalline graphene samples with four different grain sizes d after MD relaxation at 300 K and zero pressure.

B. The NEP model for carbon systems

In this work, we employ a NEP model constructed for general carbon systems [31] to describe the interatomic forces in both pristine and polycrystalline graphene. The NEP approach [23–25] provides highly accurate and efficient MLPs for general systems by training a neural network model using an evolutionary algorithm, which is a powerful black-box optimizer for real-valued optimization problems. The training process is guided by a loss function, which is a weighted sum of the root mean square errors (RMSEs) of energy, force, and virial, alongside regularization terms that help to prevent or alleviate overfitting. The RMSE of a physical quantity is calculated from the target values and predicted ones for the structures in the training data set.

A neural network model is employed to predict the site energy U_i of an atom in a structure. The energy of a structure is then calculated as a sum of the site energies of the atoms within the structure. As a typical many-body potential, the force and virial can be calculated straightforwardly [49]. The input of the neural network model is a descriptor vector which consists of a number of radial and angular components. Both the radial and angular components involve a number of radial functions,

each expressed as a linear combination of a number of basis functions based on Chebyshev polynomials. The target values in the training dataset were calculated based on quantum-mechanical density functional theory (DFT) calculations, as contributed by Rowe *et al.* in Ref. 30. For details on the various hyperparameters used to construct the NEP model based on this training data set, we refer to Ref. 31.

C. Methods for calculating the thermal conductivity

We use both the equilibrium molecular dynamics (EMD) and homogeneous non-equilibrium molecular dynamics (HNEMD) method to compute the thermal conductivity.

In the EMD method, on equilibrium state is first achieved, and then the running thermal conductivity $\kappa_{\mu\nu}(t)$ ($\mu, \nu = x, y, z$) is calculated as a function of the correlation time t according to the Green-Kubo relation [50, 51]:

$$\kappa_{\mu\nu}(t) = \frac{1}{k_B T^2 V} \int_0^t \langle J_\mu(0) J_\nu(t') \rangle_e dt'. \quad (1)$$

Here k_B is the Boltzmann constant, T is the temperature, V is the volume, and $\langle J_\mu(0) J_\nu(t') \rangle_e$ is the heat current autocorrelation function as evaluated in an equilibrium ensemble (hence the subscript “e”). The heat current J_μ can be calculated based on the general formulation for many-body potentials [49]:

$$\mathbf{J} = \sum_i \sum_{j \neq i} \mathbf{r}_{ij} \frac{\partial U_j}{\partial \mathbf{r}_{ji}} \cdot \mathbf{v}_i, \quad (2)$$

where $\mathbf{r}_{ij} \equiv \mathbf{r}_j - \mathbf{r}_i$, \mathbf{r}_i is the position of atom i , and \mathbf{v}_i is the velocity of atom i .

In the HNEMD method, an external driving force is first applied for each atom, and then the running thermal conductivity is calculated based on the following linear response relation [52, 53]

$$\langle J_\mu(t) \rangle_{ne} = TV \sum_\nu \kappa_{\mu\nu}(t) F_e^\nu, \quad (3)$$

where F_e^ν is the driving force parameter. For general many-body potentials, the driving force on atom i is formulated as [53]:

$$\mathbf{F}_i^{\text{ext}} = \mathbf{F}_e \cdot \sum_{j \neq i} \mathbf{r}_{ij} \otimes \frac{\partial U_j}{\partial \mathbf{r}_{ji}}. \quad (4)$$

This driving force directs more energetic atoms towards the heat flow direction and less energetic ones towards the opposite direction.

We used the GPUMD package [26] to perform all the MD simulations. A time step for integration of 1 fs was used throughout. In this work, we only considered

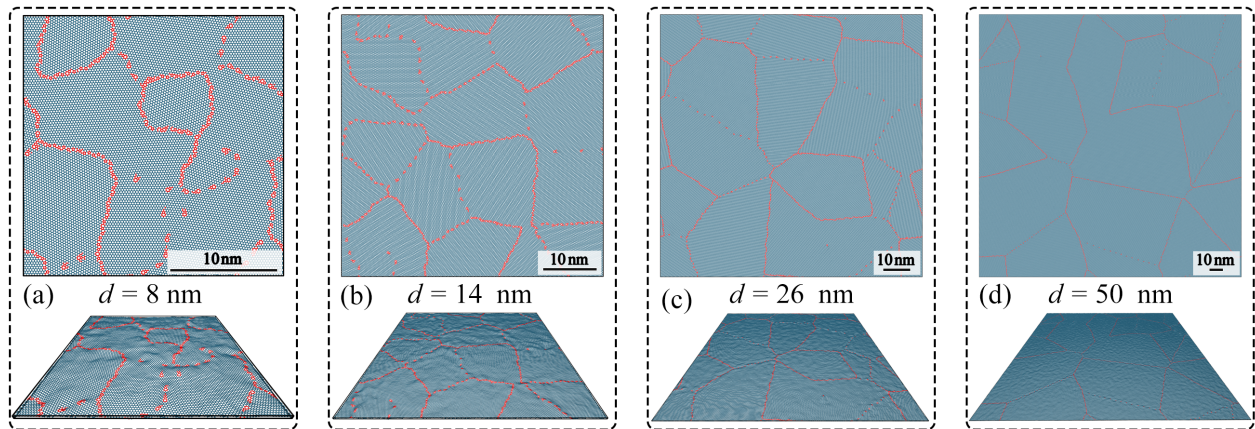


FIG. 1. Snapshots of polycrystalline graphene samples with four different grain sizes, d (where $d = (A/n)^{1/2}$, with A as the total graphene plane area and n as the number of grains), after MD relaxation at 300 K and zero pressure: (a) $d = 8$ nm (22 464 atoms), (b) $d = 14$ nm (89 858 atoms), (c) $d = 26$ nm (359 502 atoms), and (d) $d = 50$ nm (1 438 236 atoms).

the temperature of 300 K. In the HNEMD simulations, the magnitude of the driving force parameter was set to $F_e = 0.1 \mu\text{m}^{-1}$ for pristine graphene and $F_e = 1 \mu\text{m}^{-1}$ for polycrystalline graphene. To determine the volumes of the simulated systems, the layer thicknesses for both pristine graphene and polycrystalline graphene were set to 3.35 Å, corresponding to the equilibrium interlayer distance in graphite.

III. RESULTS AND DISCUSSION

A. Performance evaluation

We first evaluate the computational speed of the NEP model and compare it to several typical existing MLPs for carbon systems, including ACE [27], TurboGAP [28], PANNA [29], and GAP20 [30]. Data for the other MLPs were taken from Ref. 27. To ensure consistency with previous benchmarks [27, 28], we performed MD simulation for liquid carbon at 4000 K with a density of 2 g/cm³. Computational speed was measured as the product of the number of atoms and the number of simulation steps divided by the computation time. Most of the previous MLPs were benchmarked on CPU, with the ACE model showing the highest speed [27]. The ACE model was also benchmarked on a V100 GPU. Our NEP model demonstrates significantly higher computational speed than the ACE model, performing about 8 times faster than ACE on the same V100 GPU. Moreover, our NEP model achieves high computational performance on consumer desktop GPUs, matching the speed of V100 with an RTX 4070 and offering a two-fold speedup with an RTX 4090.

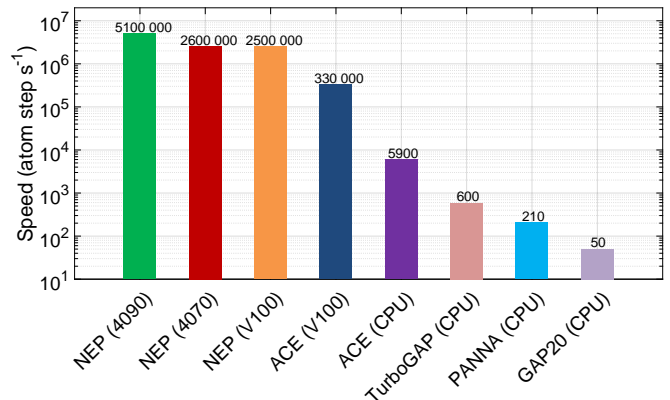


FIG. 2. Comparison of the computational speeds between NEP model and typical existing MLPs for carbon systems, including ACE [27], TurboGAP [28], PANNA [29], and GAP20 [30]. Data for MLPs other than NEP are sourced from Ref. 27. NEP outperforms the previously top-performing model, ACE, by 8x on the same V100 GPU and achieves high computational performance on consumer desktop GPUs, matching V100 speed with an RTX 4070 and delivering further 2x speedup with an RTX 4090.

B. Grain boundary energy

Before applying the NEP model to heat transport calculations, we examine the grain boundary energies, which have a strong correlation with heat transport properties [54, 55]. To this end, we use the bicrystalline graphene samples [54] previously constructed using the PFC method [48]. The grain boundary energy per unit length, or line tension γ , can be calculated as follows:

$$\gamma = \frac{E - NE_0}{2L}, \quad (5)$$

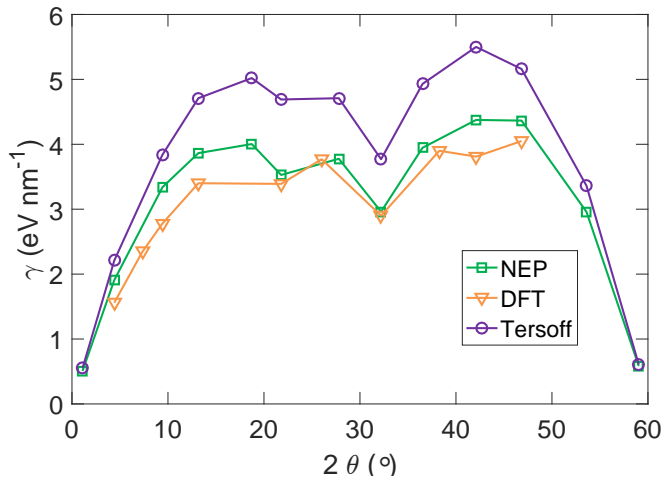


FIG. 3. Grain boundary energy density γ as a function of tilt angle 2θ , calculated using the NEP model (this work), DFT [48], and the Tersoff potential [54]. The NEP model aligns more closely with DFT calculations.

where E is the total energy of the bicrystalline graphene system with N atoms and two symmetrically tilted grain boundaries with length L , and E_0 is the energy per atom in pristine graphene. Figure 3 shows the grain boundary energy density γ as a function of the tilt angle 2θ calculated using the NEP model, compared to previous results from DFT [48] and a Tersoff potential [54]. The results from the NEP model show much better agreement with DFT calculations than the results from the Tersoff potential.

C. Thermal conductivity

After validating the NEP model's accuracy in describing the grain boundary energetics, we proceed to study the effects of grain boundary on heat transport. To this end, we employ the efficient HNEMD method to calculate the thermal conductivity of polycrystalline samples, closely comparing the results with those of pristine graphene.

Figure 4(a) presents the cumulative average of the running thermal conductivity $\kappa(t)$, as defined in Eq. (3), for pristine graphene. To facilitate the discussion, the total thermal conductivity κ^{tot} is decomposed into contributions from in-plane phonons (κ^{in}) and out-of-plane phonons (κ^{out}) [33]. For both components, the cumulative average of the running thermal conductivity converges well at a production time of 10 ns. Upon convergence, the values for pristine graphene are $\kappa^{\text{in}} = 492 \pm 11 \text{ W m}^{-1} \text{ K}^{-1}$, $\kappa^{\text{out}} = 1162 \pm 12 \text{ W m}^{-1} \text{ K}^{-1}$, and $\kappa^{\text{tot}} = 1654 \pm 23 \text{ W m}^{-1} \text{ K}^{-1}$ respectively. This indicates that the thermal conductivity of graphene is mainly contributed by the out-of-plane phonons, i.e., the flexural modes (κ^{out}). It has been observed [56] that NEP tends to slightly underestimate the thermal conductivity of typ-

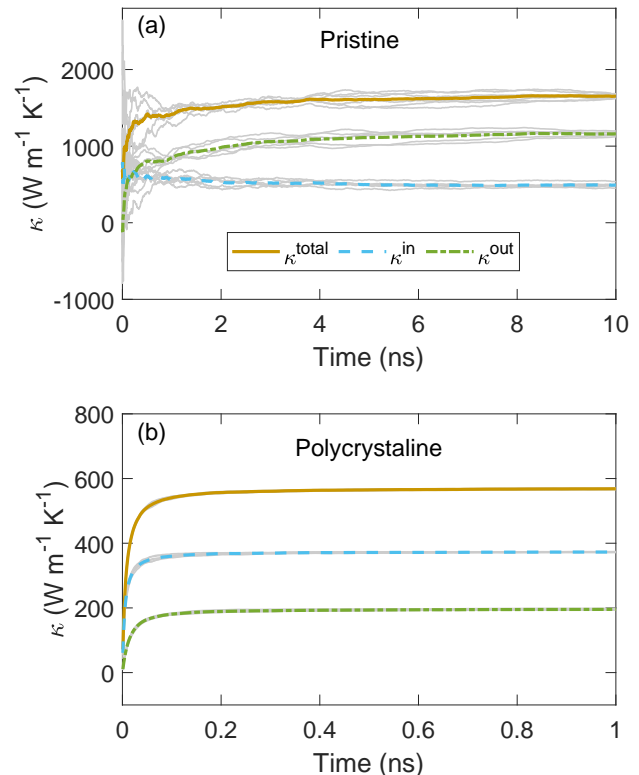


FIG. 4. Cumulative average of the running thermal conductivity, showing total (κ^{tot} , orange solid line), in-plane (κ^{in} , blue dashed line), and out-of-plane (κ^{out} , green dashed-dotted line) phonon contributions as a function of production time, calculated using the HNEMD method for (a) pristine graphene (simulation domain size: about $25 \text{ nm} \times 25 \text{ nm}$, 24 000 atoms) and (b) polycrystalline graphene (grain size: $d = 50 \text{ nm}$, 1 438 236 atoms) at 300 K and zero pressure. The thin lines represent independent runs and the thick lines show the averaged results. Six independent runs were conducted for both pristine and polycrystalline graphene.

ical materials, including pristine graphene, due to force errors, though this underestimation could be corrected systematically. However, since the focus of this work is not on the absolute values of thermal conductivity, we do not apply such corrections here.

Figure 4(b) presents the results for the polycrystalline graphene with a grain size of $d = 50 \text{ nm}$. The cumulative average of the running thermal conductivity converges well at a production time of 1 ns. Upon convergence, the values for polycrystalline graphene are $\kappa^{\text{in}} = 373 \pm 2 \text{ W m}^{-1} \text{ K}^{-1}$, $\kappa^{\text{out}} = 195 \pm 1 \text{ W m}^{-1} \text{ K}^{-1}$, and $\kappa^{\text{tot}} = 568 \pm 3 \text{ W m}^{-1} \text{ K}^{-1}$ respectively. In contrast to pristine graphene, the thermal conductivity of polycrystalline graphene is mainly contributed by the in-plane phonons (κ^{in}). Additional results for polycrystalline graphene with other grain sizes are shown in Fig. 5. As the grain size decreases, both the absolute and relative contributions of the flexural phonons to the total

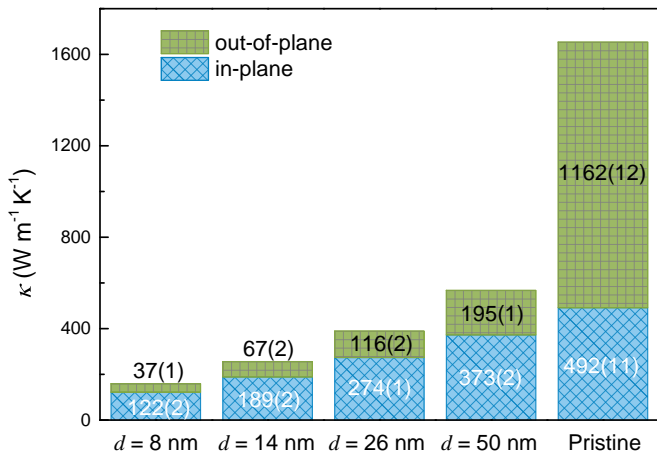


FIG. 5. In-plane (κ^{in} , lower blue bars), out-of-plane (κ^{out} , upper green bars), and total (κ^{tot} , combined blue and green bars) thermal conductivity for polycrystalline graphene with various grain sizes ($d = 8$ nm, 22 464 atoms; $d = 14$ nm, 89 858 atoms; $d = 26$ nm, 359 502 atoms; $d = 50$ nm, 1 438 236 atoms) and pristine graphene (simulation domain size: approximately $25 \text{ nm} \times 25 \text{ nm}$, 24 000 atoms) at 300 K and zero pressure.

thermal conductivity decrease.

The aforementioned results are for unstrained systems. Next, we consider the effects of external tensile strain, which is usually unavoidable and important for two-dimensional materials. Previous works [32–34] suggest that the thermal conductivity in sufficiently stretched graphene might be divergent, i.e., it increases with sample size (proportional to the correlation time in EMD) without an upper limit. This behavior is confirmed here for pristine graphene under 40 GPa biaxial tensile stress (equivalent to about 5% biaxial tensile strain), as shown in Fig. 6.

For the strained systems, the EMD method is used, as the running thermal conductivity in HNEMD simulations may also show divergence in the non-linear response regime due to an extensively large driving force parameter [53], complicating the analysis. In strained pristine graphene, the running thermal conductivity surpasses that of unstrained pristine graphene at a correlation time of about 0.01 ns and rapidly increases after a correlation time of 3 ns, showing no signs of convergence up to a correlation time of 5 ns. While our results do not definitely confirm the divergence of the thermal conductivity in strained pristine graphene at infinite correlation time, they are consistent with previous studies [32–34].

In contrast, polycrystalline graphene with grain size $d = 14$ nm shows well-converged thermal conductivity with respect to the correlation time under a 40 GPa biaxial tensile stress, with an enhanced convergent thermal conductivity of $399 \pm 21 \text{ W m}^{-1} \text{ K}^{-1}$, compared to $256 \pm 4 \text{ W m}^{-1} \text{ K}^{-1}$ under zero stress, indicating that tensile strain can enhance the thermal conductivity in both pristine and polycrystalline graphene, except

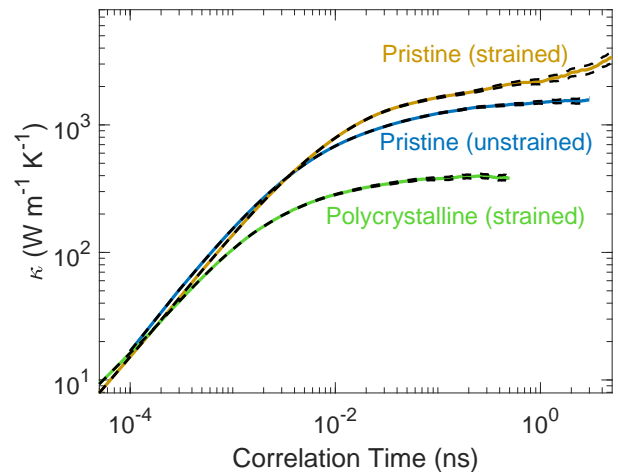


FIG. 6. Running thermal conductivity as a function of correlation time for pristine graphene under biaxial tensile strain (40 GPa stress, orange line) and without strain (blue line), and polycrystalline graphene (grain size $d = 14$ nm) under the same biaxial tensile strain (40 GPa stress, green line) at 300 K. Black dashed lines represent the error bounds calculated from the standard error based on about 100 independent EMD runs. For pristine graphene, the simulation domain size under zero pressure is about $25 \text{ nm} \times 25 \text{ nm}$. Unlike pristine graphene, polycrystalline graphene under biaxial tensile strain (40 GPa stress) at 300 K does not exhibit divergent thermal conductivity.

in small samples in the ballistic regime [57].

The finite (non-divergent) thermal conductivity in polycrystalline graphene under significant tensile strain is intriguing, as it indicates that grain boundaries, along with asymmetric interatomic interactions [35–39] and nearly integrable dynamics [40–42], may play a crucial role in thermal transport in momentum-conserving low-dimensional systems, where the foundations of the empirical Fourier’s heat conduction law remain to be rigorously established [43–46]. Further investigations are required to better understand the role of grain boundaries and explore the underlying mechanisms that could lead to Fourier’s heat conduction law in low-dimensional momentum-conserving systems.

IV. SUMMARY AND CONCLUSIONS

In this work, we employed the highly efficient NEP model, as implemented in the GPUMD package, to investigate heat transport in million-atom polycrystalline graphene, in close comparison with pristine graphene.

First, we demonstrated that the NEP model achieves computational speed at least an order of magnitude faster than state-of-the-art MLPs in the literature. The high efficiency of NEP makes fully atomistic simulation of heat transport in million-atom systems feasible.

Next, we validated that the NEP model provides signif-

icantly more accurate descriptions of grain boundary energies compared to the Tersoff potential, closely matching the results from DFT calculations. Following this validation, we calculated the thermal conductivity of pristine and polycrystalline graphene systems using the HNEMD and EMD methods.

Our results show that the grain boundaries significantly reduce the thermal conductivity of graphene, especially limiting the contribution from the out-of-plane (flexural) phonon modes. Moreover, we investigated the effects of tensile strain and found that it enhances the thermal conductivity of both pristine and polycrystalline graphene systems.

However, a key qualitative difference emerges: while the thermal conductivity in sufficiently stretched pristine graphene appears to diverge with increasing correlation time (or sample size), the thermal conductivity in similarly stretched polycrystalline graphene converges to a finite value. This suggests that grain boundaries play an important role in modulating heat transport in polycrystalline graphene under strains. It also indicates that grain boundaries, along with asymmetric interatomic interactions [35–39] and nearly integrable dynamics [40–42], may be crucial in thermal transport in low-dimensional momentum-conserving systems [43–46]. Further investigations in separate works are needed to further elucidate the role of grain boundaries and investigate the underlying mechanisms that could lead to Fourier’s heat conduction law in low-dimensional momentum-conserving systems.

Our highly efficient and accurate NEP approach enables detailed investigations of large-scale systems, providing deeper insights into heat transport in graphene

with grain boundaries and external strains. These findings will facilitate closer comparisons with experimental results, considering the ubiquitous presence of both large-scale grain boundaries and external strains in real-world materials. The capability of simulating millions of atoms with near-first-principles accuracy on consumer desktop GPUs using the NEP approach will enhance the accessibility to large-scale and accurate atomistic simulations for the broader research community, leveraging both high-performance computing resources and consumer-grade hardware.

ACKNOWLEDGMENTS

H.D. is supported by the Science Foundation from the Education Department of Liaoning Province (No. JYTMS20231613) and the Doctoral start-up Fund of Bohai University (No. 0523bs008). X.Z. is supported by the College Students’ Innovation and Entrepreneurship Training Program of Liaoning Province (No. S202410167146).

Data availability:

Complete input and output files for the general-purpose carbon NEP model are freely available at <https://gitlab.com/brucefan1983/nep-data>.

Declaration of competing interest:

The authors declare that they have no competing interests.

-
- [1] G. C. Sosso, D. Donadio, S. Caravati, J. Behler, and M. Bernasconi, Thermal transport in phase-change materials from atomistic simulations, *Phys. Rev. B* **86**, 104301 (2012).
 - [2] J. Behler and M. Parrinello, Generalized Neural-Network Representation of High-Dimensional Potential-Energy Surfaces, *Phys. Rev. Lett.* **98**, 146401 (2007).
 - [3] H. Dong, Y. Shi, P. Ying, K. Xu, T. Liang, Y. Wang, Z. Zeng, X. Wu, W. Zhou, S. Xiong, S. Chen, and Z. Fan, Molecular dynamics simulations of heat transport using machine-learned potentials: A mini-review and tutorial on GPUMD with neuroevolution potentials, *Journal of Applied Physics* **135**, 161101 (2024).
 - [4] R. Cheng, X. Shen, S. Klotz, Z. Zeng, Z. Li, A. Ivanov, Y. Xiao, L.-D. Zhao, F. Weber, and Y. Chen, Lattice dynamics and thermal transport of PbTe under high pressure, *Physical Review B* **108**, 104306 (2023).
 - [5] P.-H. Du, C. Zhang, T. Li, and Q. Sun, Low lattice thermal conductivity with two-channel thermal transport in the superatomic crystal PH₄AlBr₄, *Physical Review B* **107**, 155204 (2023).
 - [6] P. Ying, T. Liang, K. Xu, J. Zhang, J. Xu, Z. Zhong, and Z. Fan, Sub-micrometer phonon mean free paths in metal-organic frameworks revealed by machine-learning molecular dynamics simulations, *ACS Applied Materials & Interfaces* **15**, 36412 (2023).
 - [7] X. Wang, J. Yang, P. Ying, Z. Fan, J. Zhang, and H. Sun, Dissimilar thermal transport properties in κ -Ga₂O₃ and β -Ga₂O₃ revealed by homogeneous nonequilibrium molecular dynamics simulations using machine-learned potentials, *Journal of Applied Physics* **135**, 065104 (2024).
 - [8] M. Zeraati, A. R. Oganov, T. Fan, and S. F. Solodovnikov, Searching for low thermal conductivity materials for thermal barrier coatings: A theoretical approach, *Phys. Rev. Mater.* **8**, 033601 (2024).
 - [9] H. Dong, C. Cao, P. Ying, Z. Fan, P. Qian, and Y. Su, Anisotropic and high thermal conductivity in monolayer quasi-hexagonal fullerene: A comparative study against bulk phase fullerene, *International Journal of Heat and Mass Transfer* **206**, 123943 (2023).
 - [10] W. Sha, X. Dai, S. Chen, B. Yin, and F. Guo, Phonon thermal transport in two-dimensional PbTe monolayers via extensive molecular dynamics simulations with a neuroevolution potential, *Materials Today Physics* **34**, 101066 (2023).

- [11] F. Eriksson, E. Fransson, C. Linderålv, Z. Fan, and P. Erhart, Tuning the through-plane lattice thermal conductivity in van der waals structures through rotational (dis) ordering, *ACS Nano* **17**, 25565–25574 (2023).
- [12] G. Li, J. Tang, J. Zheng, Q. Wang, Z. Cui, K. Xu, J. Xu, T.-H. Liu, G. Zhu, R. Guo, and B. Li, Convergent thermal conductivity in strained monolayer graphene, *Phys. Rev. B* **109**, 035420 (2024).
- [13] Z. Li, H. Dong, J. Wang, L. Liu, and J.-Y. Yang, Active learning molecular dynamics-assisted insights into ultralow thermal conductivity of two-dimensional covalent organic frameworks, *International Journal of Heat and Mass Transfer* **225**, 125404 (2024).
- [14] Y. Wang, Z. Fan, P. Qian, M. A. Caro, and T. Ala-Nissila, Quantum-corrected thickness-dependent thermal conductivity in amorphous silicon predicted by machine learning molecular dynamics simulations, *Physical Review B* **107**, 054303 (2023).
- [15] H. Zhang, X. Gu, Z. Fan, and H. Bao, Vibrational anharmonicity results in decreased thermal conductivity of amorphous HfO_2 at high temperature, *Physical Review B* **108**, 045422 (2023).
- [16] T. Liang, P. Ying, K. Xu, Z. Ye, C. Ling, Z. Fan, and J. Xu, Mechanisms of temperature-dependent thermal transport in amorphous silica from machine-learning molecular dynamics, *Phys. Rev. B* **108**, 184203 (2023).
- [17] Y. Li, Y. Guo, S. Xiong, and H. Yi, Enhanced heat transport in amorphous silicon via microstructure modulation, *International Journal of Heat and Mass Transfer* **222**, 125167 (2024).
- [18] P. Pegolo and F. Grasselli, Thermal transport of glasses via machine learning driven simulations, *Frontiers in Materials* **11**, 1369034 (2024).
- [19] D. Tisi, L. Zhang, R. Bertossa, H. Wang, R. Car, and S. Baroni, Heat transport in liquid water from first-principles and deep neural network simulations, *Physical Review B* **104**, 224202 (2021).
- [20] K. Xu, Y. Hao, T. Liang, P. Ying, J. Xu, J. Wu, and Z. Fan, Accurate prediction of heat conductivity of water by a neuroevolution potential, *The Journal of Chemical Physics* **158** (2023).
- [21] C. Mangold, S. Chen, G. Barbalinardo, J. Behler, P. Pochet, K. Termentzidis, Y. Han, L. Chaput, D. Lacroix, and D. Donadio, Transferability of neural network potentials for varying stoichiometry: Phonons and thermal conductivity of Mn_xGe_y compounds, *Journal of Applied Physics* **127**, 244901 (2020).
- [22] J. Wu, E. Zhou, A. Huang, H. Zhang, M. Hu, and G. Qin, Deep-potential enabled multiscale simulation of gallium nitride devices on boron arsenide cooling substrates, *Nature Communications* **15**, 2540 (2024).
- [23] Z. Fan, Z. Zeng, C. Zhang, Y. Wang, K. Song, H. Dong, Y. Chen, and T. Ala-Nissila, Neuroevolution machine learning potentials: Combining high accuracy and low cost in atomistic simulations and application to heat transport, *Phys. Rev. B* **104**, 104309 (2021).
- [24] Z. Fan, Improving the accuracy of the neuroevolution machine learning potential for multi-component systems, *Journal of Physics: Condensed Matter* **34**, 125902 (2022).
- [25] Z. Fan, Y. Wang, P. Ying, K. Song, J. Wang, Y. Wang, Z. Zeng, K. Xu, E. Lindgren, J. M. Rahm, A. J. Gabourie, J. Liu, H. Dong, J. Wu, Y. Chen, Z. Zhong, J. Sun, P. Erhart, Y. Su, and T. Ala-Nissila, GPUMD: A package for constructing accurate machine-learned potentials and performing highly efficient atomistic simulations, *The Journal of Chemical Physics* **157**, 114801 (2022).
- [26] Z. Fan, W. Chen, V. Vierimaa, and A. Harju, Efficient molecular dynamics simulations with many-body potentials on graphics processing units, *Computer Physics Communications* **218**, 10 (2017).
- [27] M. Qamar, M. Mrovec, Y. Lysogorskiy, A. Bochkarev, and R. Drautz, Atomic cluster expansion for quantum-accurate large-scale simulations of carbon, *Journal of Chemical Theory and Computation* **19**, 5151 (2023).
- [28] Y. Wang, Z. Fan, P. Qian, T. Ala-Nissila, and M. A. Caro, Structure and pore size distribution in nanoporous carbon, *Chemistry of Materials* **34**, 617 (2022).
- [29] Y. Shaidu, E. Küçükbenli, R. Lot, F. Pellegrini, E. Kaxiras, and S. de Gironcoli, A systematic approach to generating accurate neural network potentials: The case of carbon, *npj Computational Materials* **7**, 52 (2021).
- [30] P. Rowe, V. L. Deringer, P. Gasparotto, G. Csányi, and A. Michaelides, An accurate and transferable machine learning potential for carbon, *The Journal of Chemical Physics* **153**, 034702 (2020).
- [31] Z. Fan, Y. Xiao, Y. Wang, P. Ying, S. Chen, and H. Dong, Combining linear-scaling quantum transport and machine-learning molecular dynamics to study thermal and electronic transports in complex materials, *Journal of Physics: Condensed Matter* **36**, 245901 (2024).
- [32] L. F. C. Pereira and D. Donadio, Divergence of the thermal conductivity in uniaxially strained graphene, *Phys. Rev. B* **87**, 125424 (2013).
- [33] Z. Fan, L. F. C. Pereira, P. Hirvonen, M. M. Ervasti, K. R. Elder, D. Donadio, T. Ala-Nissila, and A. Harju, Thermal conductivity decomposition in two-dimensional materials: Application to graphene, *Phys. Rev. B* **95**, 144309 (2017).
- [34] M. Xu, Anomalous size effect of thermal conductivity of two-dimensional dielectric materials, *Physica Scripta* **98**, 115951 (2023).
- [35] Y. Zhong, Y. Zhang, J. Wang, and H. Zhao, Normal heat conduction in one-dimensional momentum conserving lattices with asymmetric interactions, *Phys. Rev. E* **85**, 060102 (2012).
- [36] S. Chen, Y. Zhang, J. Wang, and H. Zhao, Breakdown of the power-law decay prediction of the heat current correlation in one-dimensional momentum conserving lattices (2012), arXiv:1204.5933 [cond-mat.stat-mech].
- [37] S. Chen, Y. Zhang, J. Wang, and H. Zhao, Why asymmetric interparticle interaction can result in convergent heat conductivity (2013), arXiv:1309.7146 [cond-mat.stat-mech].
- [38] S. Chen, J. Wang, G. Casati, and G. Benenti, Thermoelectricity of interacting particles: A numerical approach, *Phys. Rev. E* **92**, 032139 (2015).
- [39] S. Chen, Y. Zhang, J. Wang, and H. Zhao, Key role of asymmetric interactions in low-dimensional heat transport, *Journal of Statistical Mechanics: Theory and Experiment*, 033205 (2016).
- [40] S. Chen, J. Wang, G. Casati, and G. Benenti, Nonintegrability and the fourier heat conduction law, *Phys. Rev. E* **90**, 032134 (2014).
- [41] H. Zhao and W.-g. Wang, Fourier heat conduction as a strong kinetic effect in one-dimensional hard-core gases, *Phys. Rev. E* **97**, 010103 (2018).
- [42] S. Lepri, R. Livi, and A. Politi, Too close to inte-

- grable: Crossover from normal to anomalous heat diffusion, *Phys. Rev. Lett.* **125**, 040604 (2020).
- [43] F. Bonetto, J. L. Lebowitz, and L. Rey-Bellet, Fourier's law: A challenge to theorists, in *Mathematical Physics 2000*, pp. 128–150.
- [44] S. Lepri, R. Livi, and A. Politi, Thermal conduction in classical low-dimensional lattices, *Physics Reports* **377**, 1 (2003).
- [45] A. Dhar, Heat transport in low-dimensional systems, *Advances in Physics* **57**, 457 (2008).
- [46] G. Benenti, D. Donadio, S. Lepri, and R. Livi, Non-Fourier heat transport in nanosystems, *La Rivista del Nuovo Cimento* **46**, 105 (2023).
- [47] Z. Fan, P. Hirvonen, L. F. C. Pereira, M. M. Ervasti, K. R. Elder, D. Donadio, A. Harju, and T. Ala-Nissila, Bimodal Grain-Size Scaling of Thermal Transport in Polycrystalline Graphene from Large-Scale Molecular Dynamics Simulations, *Nano Letters* **17**, 5919 (2017).
- [48] P. Hirvonen, M. M. Ervasti, Z. Fan, M. Jalalvand, M. Seymour, S. M. Vaez Allaei, N. Provatas, A. Harju, K. R. Elder, and T. Ala-Nissila, Multiscale modeling of polycrystalline graphene: A comparison of structure and defect energies of realistic samples from phase field crystal models, *Phys. Rev. B* **94**, 035414 (2016).
- [49] Z. Fan, L. F. C. Pereira, H.-Q. Wang, J.-C. Zheng, D. Donadio, and A. Harju, Force and heat current formulas for many-body potentials in molecular dynamics simulations with applications to thermal conductivity calculations, *Phys. Rev. B* **92**, 094301 (2015).
- [50] M. S. Green, Markoff Random Processes and the Statistical Mechanics of Time-dependent Phenomena. II. Irreversible Processes in Fluids, *The Journal of Chemical Physics* **22**, 398 (1954).
- [51] R. Kubo, Statistical-Mechanical Theory of Irreversible Processes. I. General Theory and Simple Applications to Magnetic and Conduction Problems, *Journal of the Physical Society of Japan* **12**, 570 (1957).
- [52] D. J. Evans, Homogeneous NEMD algorithm for thermal conductivity—Application of non-canonical linear response theory, *Physics Letters A* **91**, 457 (1982).
- [53] Z. Fan, H. Dong, A. Harju, and T. Ala-Nissila, Homogeneous nonequilibrium molecular dynamics method for heat transport and spectral decomposition with many-body potentials, *Phys. Rev. B* **99**, 064308 (2019).
- [54] K. Azizi, P. Hirvonen, Z. Fan, A. Harju, K. R. Elder, T. Ala-Nissila, and S. M. V. Allaei, Kapitza thermal resistance across individual grain boundaries in graphene, *Carbon* **125**, 384 (2017).
- [55] H. Dong, P. Hirvonen, Z. Fan, and T. Ala-Nissila, Heat transport in pristine and polycrystalline single-layer hexagonal boron nitride, *Phys. Chem. Chem. Phys.* **20**, 24602 (2018).
- [56] X. Wu, W. Zhou, H. Dong, P. Ying, Y. Wang, B. Song, Z. Fan, and S. Xiong, Correcting force error-induced underestimation of lattice thermal conductivity in machine learning molecular dynamics, *The Journal of Chemical Physics* **161**, 014103 (2024).
- [57] N. Wei, L. Xu, H.-Q. Wang, and J.-C. Zheng, Strain engineering of thermal conductivity in graphene sheets and nanoribbons: a demonstration of magic flexibility, *Nanotechnology* **22**, 105705 (2011).